Progress In Electromagnetics Research, PIER 11, 255–300, 1995

FINITE-DIFFERENCE TIME-DOMAIN METHOD FOR OPTICAL WAVEGUIDE ANALYSIS

S. T. Chu and S. K. Chaudhuri

1. Introduction

The preceding chapters have described a number of frequency domain methods that study the behavior of monochromatic wave propagation in optical waveguides. In this chapter, an alternate approach to numerical guided-wave optics modeling, the finite-difference time-domain (FDTD) method will be described. The FDTD method is a direct solution to Maxwell's time-dependent curl equations and it differs from the previous methods in the sense that it solves the problem

in the time-domain. It will be shown in the following sections that by including the time dependence in the analysis, the FDTD method can incorporate the effects of reflection and radiation that are commonly neglected by other methods. The FDTD method can also model wave propagation in complex media, such as time-varying, anisotropic, lossy, dispersive, and nonlinear media.

Although the FDTD method was first proposed in 1966 by Yee [1] to solve problems in electromagnetic scattering, it has not until the mid-seventies, when computational power became more accessible, that the method started to gain popularity in the area of microwave and millimeter-wave research. With the continual advances in computer research and the reduction of computational costs, the FDTD method is being applied at problem associated with increasingly higher frequencies, from microwave to millimeter-wave to optics. There is a strong possibility that the FDTD method will become one of the most versatile and powerful methods in solving problems involving electromagnetic wave interactions.

In this chapter we are concerned mainly with applying the FDTD method to solve optical waveguide problems. Along with the basic Yee formulations, recent advances in FDTD formulations for more complex media will be presented. We will introduce two alternate approaches that are more computationally efficient and which maintain the same degree of accuracy when applied to two-dimensional problems or in the analysis of weakly guiding structures. Even though the FDTD method does demand relatively high computational resources and using it to solve optically large structures may be expensive, there are certain optical devices of current interest whose development can benefit from the FDTD analysis. We will address the applicability issues in latter part of the chapter. With this in mind, an overview of the FDTD method will be given in section 2 which will describe the development of the FDTD method; the general characteristics and the operational principles of the method will also be discussed. The overview is designed specifically for readers whose interest is to obtain general understanding of the FDTD method without having to delving into the mathematics. In section 3, the basic FDTD algorithm will be presented in detail. The basic algorithm deals with wave propagation in linear, lossless, and nondispersive media. Here, the behavior of the wave propagator, such as numerical stability and numerical dispersion, will be discussed. The implementation details, such as on the excitation of input signal

and on the handling of outgoing wave at the external boundary will be provided.

The alternate approaches will be presented in Section 4. The motivation for the development of the scalar and semi-vectorial FDTD methods will be addressed first, which will be followed by the formulation and limitations of the alternative approaches. Section 5 emphasizes the modifications to the basic FDTD algorithm when applied to more complex media, such as dispersive and time varying media. Examples of the FDTD simulation will also be provided.

The method has recently been extended to analyze wave propagation in nonlinear medium. However, this subject is out of the scope of this book and interested readers should consult the works of Goorjian and Taflove [2,3], and Ziolkowski [4]. In the conclusion, we will discuss research trends on the FDTD algorithm in optics and the type of structures whose analysis can be benefited from the FDTD analysis.

2. Overview of the FDTD Method

The FDTD method was initially used by Yee [1] for analyzing the two-dimensional problem of the scattering of transverse magnetic (TM) pulses from rectangular cylindrical conductors. The method was later extended to three dimensional cases with steady-state excitation by Taflove and Brodwin [5]. With the increase in computational power of the late seventies, larger and more complex problems have been solved by the FDTD method. The method has been applied to a number of problems in the area of microwave and millimeter wave research [6–11]. As the integrated optical circuits (IOCs) become more compact, the FDTD method becomes more applicable to the analysis of these IOCs [12–17]. The validity of the FDTD method for optical waveguide analysis was investigated by Chu and Chaudhuri [12]. It has been applied to characterize fast photoconductive switches [18], to the analysis of roughsurface effects in mirrors [15], and to the characterization of planar fluorescence sensors. It has recently been extended to study problems involving ultrafast pulse propagation in nonlinear media [2,3].

Similar to the beam propagation method (BPM), the FDTD method also models the propagation of an incident electromagnetic wave into a volume of space containing the structure of interest. The FDTD algorithm, however, is based on the finite difference expression

of the set of Maxwell's equations instead of the one-way wave equation in the BPM. Thus, the FDTD wave propagator involves marching in time rather than marching in space as is the BPM.

In Cartesian coordinates, the FDTD propagator is formulated by discretizing the volume into cells. As an example, the Yee lattice where the components of $\overrightarrow{E}$ and $\overrightarrow{H}$ are positioned at alternate half intervals is shown in Fig. 1. The discretization of the coupled Maxwell's time-dependent curl equations is done by solving them using the leap-frog method [19], where the $\overrightarrow{E}$ and $\overrightarrow{H}$ and fields are evaluated at alternate half time steps. The central difference form, which attains a second order accuracy in the discretization interval, is used to represent the partial derivatives in the curl equations. By repeatedly applying the propagator, the incident wave can then be tracked as it passes through the volume. The wave-tracking is completed when the steady-state or the late-time behavior are observed at the sampling location. The result is a set of complete field descriptions that contain the solution to the problem within the volume at the sampling time intervals.

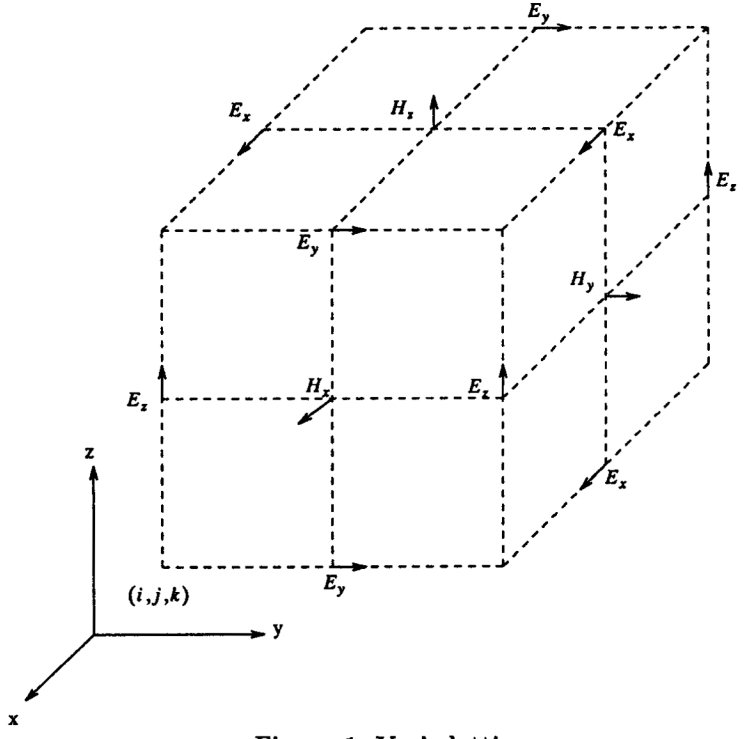

Figure 1. Yee's lattice.

The advantages of the FDTD method are its simplicity and its versatility. By formulating the computational procedure locally and time-explicitly, the complete interaction between the incident wave and the geometry can be analyzed portion by portion at any given time. The localization of the procedure allows the analysis to be performed without having to find the simultaneous solution to the entire problem. Furthermore, the curl equations generate the boundary conditions at the media interfaces so that no special treatment is needed at these interfaces. The above features, combined with the discretization of the structure of interest, allow the FDTD method to solve a very large class of problems, including arbitrarily shaped or profiled complex structures which may involve electrically or magnetically anisotropic media.

In the computer implementation of the FDTD method, the storage and run-time increase linearly with N, the number of unknown field components in the set of $\overrightarrow{E}$ and $\overrightarrow{H}$ fields. Implicit techniques, such as the moment method using the volume integral formulation, require storage and run-time proportional to N^2. The explicit scheme is well suited for parallel processing and vectorization. The FDTD algorithm takes full advantage of machines that can provide these special functions. When applying the FDTD method in solving optical waveguide problems, the following considerations should be taken into account:

i) In optical waveguide structures, as shown in Fig 2, where the guided waves propagate along the axial direction with the decaying transverse field extending to infinity, the waves will glance off the side-boundaries of the computation region but arrive at the end-boundary broadside. It is necessary to formulate boundary conditions at these planes so that they will only absorb incoming waves without generating any spurious reflection that can affect the solutions. In general, absorption at the side-boundaries is difficult and absorption at the end-boundaries is easier.

ii) The FDTD algorithm is the solution to an initial value problem and it requires an excitation scheme to start the simulation. Although the excitation can be of the form of a point source or a plane wave, the incident wave in most optical waveguide problems generally has the form of a guided mode. A poor excitation scheme will generate unwanted transient and backward propagating parasitic waves which can create noise problems.

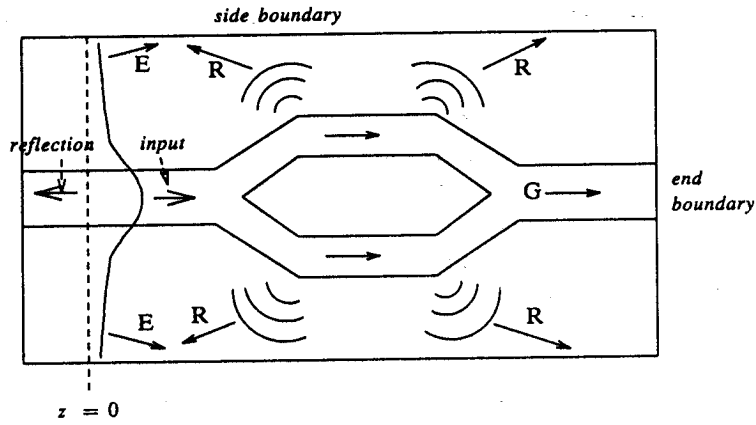

Figure 2. A typical optical waveguide structure.

iii) Typically, the waveform at the waveguide output is the superposition of a finite number of guided modes and a continuous spectrum of radiation modes. In order to determine the amount of guided power in the waveguide, one can extend the computation region until all the radiations are detached, with only the guided modes remaining in the waveguides. However, this process adds an extra burden on the computation resources. A procedure that can separate the amount of guided power from the total power in the near field would be beneficial.

iv) The solution in the frequency domain is usually obtained by using a single frequency continuous wave (CW) excitation and is determined from the steady-state field values. However, it is also possible to simulate a pulse propagating through the structure and then obtain the frequency domain solution from the time domain solution. The solutions obtained from the two types of simulations may disagree; the difference originates from the discretization size. Since the pulse is a broadband signal and provides the frequency domain result through discrete fast Fourier transform (FFT) of the time domain result, it is more susceptible to numerical dispersion and numerical noise.

v) The minimum waveguide wavelength in the structure must be estimated to determine the number of sampling points per wavelength; otherwise, the waveform will disperse as it propagates along the waveguide. The topic of numerical dispersion will be discussed in 3.4.

3. Formulation and Implementation in Cartesian Coordinate

In the following sections, the FDTD formulation in Cartesian coordinates for a linear and nondispersive medium will be presented. We will use this basic formulation to illustrate the various features of the FDTD algorithm. We will also discuss the error behaviors and pointers for implementing the FDTD method in optical waveguide analysis.

3.1 Basic Formulation.

Consider a linear medium in which the property tensors, the permittivity tensor $\overleftrightarrow{\epsilon}$, the permeability tensor $\overleftrightarrow{\mu}$, and the conductivity tensor a are time independent. Using the MKS system of units, Maxwell's time dependent curl equations in the medium are:

$$\nabla \times \vec{\boldsymbol{\varepsilon}} = -\overleftrightarrow{\mu} \frac{\partial \overrightarrow{\mathcal{H}}}{\partial t} \tag{1}$$

$$\nabla \times \overrightarrow{\mathcal{H}} = \overleftrightarrow{\epsilon} \frac{\partial \vec{\boldsymbol{\varepsilon}}}{\partial t} + \overleftrightarrow{\sigma}\ \vec{\boldsymbol{\varepsilon}} \tag{2}$$

where $\vec{\boldsymbol{\varepsilon}}$ and $\overrightarrow{\mathcal{H}}$ are the electric and magnetic field vectors, respectively. We will normalize $\vec{\boldsymbol{\varepsilon}}$ and $\overrightarrow{\mathcal{H}}$ as follows:

$$\vec{\boldsymbol{\varepsilon}} = \sqrt{\mu_0}\ \overrightarrow{E} \tag{3}$$

$$\overrightarrow{\mathcal{H}} = \sqrt{\epsilon_0}\ \overrightarrow{H} \tag{4}$$

The magnitudes of the normalized fields $\overrightarrow{E}$ and $\overrightarrow{H}$ are now of the same order. This reduces the amount of truncation and the round-off errors during the computation procedure. Substituting the set of normalized fields into (1) and (2) results in:

$$\nabla \times \overrightarrow{E} = -\overleftrightarrow{\mu}_r \frac{\partial \overrightarrow{H}}{\partial \tau} \tag{5}$$

$$\nabla \times \overrightarrow{H} = \overleftrightarrow{\epsilon}_r \frac{\partial \overrightarrow{E}}{\partial \tau} + \overleftrightarrow{\sigma}\ Z_0\ \overrightarrow{E} \tag{6}$$

where $\tau = ct$, $\overleftrightarrow{\epsilon}_r = \overleftrightarrow{\epsilon} / \epsilon_0$ and $\overleftrightarrow{\epsilon} = \overleftrightarrow{\mu} / \mu_0$ are, respectively, the relative permittivity and permeability tensors. $Z_0 = (\mu_0/\epsilon_0)^{1/2}$ is the free-space impedance, and $c = (\epsilon_0 \mu_0)^{-1/2}$ is the velocity of light in free-space.

In the Cartesian coordinate system, if we assume the principal axes of the property tensors of the medium are aligned with the axes of the coordinate, that is,

$$\overleftrightarrow{\epsilon}_r = \begin{vmatrix} \epsilon_{xx} & 0 & 0 \\ 0 & \epsilon_{yy} & 0 \\ 0 & 0 & \epsilon_{zz} \end{vmatrix}, \qquad \overleftrightarrow{\mu}_r = \begin{vmatrix} \mu_{xx} & 0 & 0 \\ 0 & \mu_{yy} & 0 \\ 0 & 0 & \mu_{zz} \end{vmatrix}$$

and

$$\overleftrightarrow{\sigma} = \begin{vmatrix} \sigma_{xx} & 0 & 0 \\ 0 & \sigma_{yy} & 0 \\ 0 & 0 & \sigma_{zz} \end{vmatrix} \tag{7}$$

then the Cartesian component form of the normalized curl equations is:

$$\frac{\partial H_x}{\partial \tau} = \frac{1}{\mu_{xx}} \left[\frac{\partial E_y}{\partial z} - \frac{\partial E_z}{\partial y} \right] \tag{8}$$

$$\frac{\partial H_y}{\partial \tau} = \frac{1}{\mu_{yy}} \left[\frac{\partial E_z}{\partial x} - \frac{\partial E_x}{\partial z} \right] \tag{9}$$

$$\frac{\partial H_z}{\partial \tau} = \frac{1}{\mu_{zz}} \left[\frac{\partial E_x}{\partial y} - \frac{\partial E_y}{\partial x} \right] \tag{10}$$

$$\frac{\partial E_x}{\partial \tau} = \frac{1}{\epsilon_{xx}} \left[\frac{\partial H_z}{\partial y} - \frac{\partial H_y}{\partial z} - \sigma_{xx} Z_0 E_x \right] \tag{11}$$

$$\frac{\partial E_y}{\partial \tau} = \frac{1}{\epsilon_{yy}} \left[\frac{\partial H_x}{\partial z} - \frac{\partial H_z}{\partial x} - \sigma_{yy} Z_0 E_y \right] \tag{12}$$

$$\frac{\partial E_z}{\partial \tau} = \frac{1}{\epsilon_{xx}} \left[\frac{\partial H_y}{\partial x} - \frac{\partial H_x}{\partial y} - \sigma_{zz} Z_0 E_x \right] \tag{13}$$

In order to solve the set of equations (8) to (13), Yee introduced the leap-frog schemes. Following Yee's notation, we represent a point in space in the lattice by

$$(x, y, z) = (i\Delta x, j\Delta y, k\Delta z) = (i, j, k) \tag{14}$$

and a function of space and time by

$$f(x,y,z;t) = f(i\Delta x, j\Delta y, k\Delta z; n\Delta t) = f^n(i,j,k) \tag{15}$$

where $\Delta x, \Delta y$, and Δz are the space increments, Δt is the time increment and i, j, k and n are integers. The space and time derivatives in the set of Eqs. (8) to (13) can then be expressed in the centered difference form. The advantage of using the centered difference form is that the expression is second-order accurate in the discretized increment. The difference equations for $\frac{\partial f}{\partial x}$ and $\frac{\partial f}{\partial t}$ are:

$$\frac{\partial f^n(i,j,k)}{\partial x} = \frac{f^n(i+1/2,j,k) - f^n(i-1/2,j,k)}{\Delta x} + O(\Delta x^2) \tag{16}$$

$$\frac{\partial f^n(i,j,k)}{\partial t} = \frac{f^{n+1/2}(i,j,k) - f^{n-1/2}(i,j,k)}{\Delta t} + O(\Delta t^2) \tag{17}$$

The accuracy of (16) and (17) is utilized in the FDTD scheme by positioning the field components as shown in Fig. 1 and evaluating the $\overrightarrow{E}$ and $\overrightarrow{H}$ fields at alternate half time steps. Expressing the partial derivatives in (8) to (13) by the centered expressions of (16) and (17) results in the following system of finite-difference equations:

$$\begin{aligned} H_x^{n+1/2}(i,j+1/2,k+1/2) &= H_x^{n-1/2}(i,j+1/2,k+1/2) \\ &+ \frac{c\Delta t}{\mu_{xx}(i,j+1/2,k+1/2)} \\ &\cdot\left[\frac{E_y^n(i,j+1/2,k+1) - E_y^n(i,j+1/2,k)}{\Delta z}\right. \\ &\left. - \frac{E_z^n(i,j+1,k+1/2) - E_z^n(i,j,k+1/2)}{\Delta y}\right] \end{aligned} \tag{18}$$

$$\begin{aligned} H_y^{n+1/2}(i+1/2,j,k+1/2) &= H_y^{n-1/2}(i+1/2,j,k+1/2) \\ &+ \frac{c\Delta t}{\mu_{yy}(i+1/2,j,k+1/2)} \\ &\cdot\left[\frac{E_z^n(i+1,j,k+1/2) - E_z^n(i,j,k+1/2)}{\Delta x}\right. \\ &\left. - \frac{E_x^n(i+1/2,j,k+1) - E_x^n(i+1/2,j,k)}{\Delta z}\right] \end{aligned} \tag{19}$$

$$H_z^{n+1/2}(i+1/2,j+1/2,k) = H_z^{n-1/2}(i+1/2,j+1/2,k) + \frac{c\Delta t}{\mu_{zz}(i+1/2,j+1/2,k)} \cdot \left[\frac{E_x^n(i+1/2,j+1,k) - E_x^n(i+1/2,j,k)}{\Delta y} - \frac{E_y^n(i+1,j+1/2,k) - E_y^n(i,j+1/2,k)}{\Delta x} \right] \tag{20}$$

$$E_x^{n+1}(i+1/2,j,k) = \frac{M_x^-(i+1/2,j,k)}{M_x^+(i+1/2,j,k)} E_x^n(i+1/2,j,k) + \frac{c\Delta t}{\epsilon_{xx}(i+1/2,j,k) M_x^+(i+1/2,j,k)} \cdot \left[\frac{H_z^{n+1/2}(i+1/2,j+1/2,k) - H_z^{n+1/2}(i+1/2,j-1/2,k)}{\Delta y} - \frac{H_y^{n+1/2}(i+1/2,j,k+1/2) - H_y^{n+1/2}(i+1/2,j,k-1/2)}{\Delta z} \right] \tag{21}$$

$$E_y^{n+1}(i,j+1/2,k) = \frac{M_y^-(i,j+1/2,k)}{M_y^+(i,j+1/2,k)} E_y^n(i,j+1/2,k) + \frac{c\Delta t}{\epsilon_{yy}(i,j+1/2,k) M_x^+(i,j+1/2,k)} \cdot \left[\frac{H_x^{n+1/2}(i,j+1/2,k+1/2) - H_x^{n+1/2}(i,j+1/2,k-1/2)}{\Delta z} - \frac{H_z^{n+1/2}(i+1/2,j+1/2,k) - H_z^{n+1/2}(i-1/2,j+1/2,k)}{\Delta x} \right] \tag{22}$$

$$E_z^{n+1}(i,j,k+1/2) = \frac{M_z^-(i,j,k+1/2)}{M_z^+(i,j,k+1/2)} E_z^n(i,j,k+1/2)$$
$$+ \frac{c\Delta t}{\epsilon_{zz}(i,j,k+1/2) M_z^+(i,j,k+1/2)}$$
$$\cdot \left[\frac{H_y^{n+1/2}(i+1/2,j,k+1/2) - H_x^{n+1/2}(i-1/2,j,k+1/2)}{\Delta x} \right.$$
$$\left. - \frac{H_x^{n+1/2}(i,j+1/2,k+1/2) - H_x^{n+1/2}(i,j-1/2,k+1/2)}{\Delta y} \right] \tag{23}$$

where

$$M_l^{\pm}(i,j,k) = 1 \pm \frac{\sigma_{ll}(i,j,k) c\Delta t}{2\epsilon_{ll}(i,j,k)} Z_0, \quad \text{and} \quad l = x,y,z \tag{24}$$

The system of Eqs. (18) to (23) will be called the FDTD *propagator*. The function of the propagator is to transform the field distribution within the computation region from $t = n$ to $t = n+1$.

Notice that the material properties ϵ_r, and σ are related to the components of the $\overrightarrow{E}$ field difference equations, and μ_r, is associated with the $\overrightarrow{H}$ field difference equations. For example, E_x is dependent on ϵ_{xx} and σ_{xx}, and H_x is dependent only on μ_{xx}. The FDTD procedure can be applied to the anisotropic situations directly, with the structure geometry defined by specifying the material properties at the locations of the field components. Although $\overleftrightarrow{\epsilon}$, $\overleftrightarrow{\sigma}$, and $\overleftrightarrow{\mu}$ are not specified at the same spatial point, since E and H are spatially separated, this poses no problem when nonmagnetic materials are considered.

3.2 Time Marching.

The operation of the propagator can be described as follows. For $t \leq n$, assume that the field distributions $\overrightarrow{E}(\vec{r})$ and $\overrightarrow{H}(\vec{r})$ are known everywhere within the region. The components of the $\overrightarrow{H}$ field at $t = n+1/2$ can be evaluated by updating their values at $t = n-1/2$ by using the time derivative of $\overrightarrow{H}$, $\frac{\partial \overrightarrow{H}}{\partial \tau}$, at $t = n$. Since $\frac{\partial \overrightarrow{H}}{\partial \tau}$ is

related to the space derivatives of $\vec{E}$ by the curl equations, $\frac{\partial \vec{H}}{\partial \tau}$ at $t = n$ can be determined from the known values of $\vec{E}$ at $t = n$, thus resulting in (18) to (20). The calculation of $\vec{E}$ at $t = n + 1$ is performed using (21) to (23). The algorithm repeats the same process, with $\vec{E}$ and $\vec{H}$ interchanged, and with $\vec{H}$ at $t = n + 1/2$ given.

The simulation of wave propagation is performed by repeatedly implementing the propagator. Notice that the field component at a given location and time is a function of its adjacent field components in the lattice at half a time step earlier. For example, $H_x^{n+1/2}(i, j + 1/2, k + 1/2)$ in (18) is a function of $E_y^n(i, j + 1/2, k + 1), E_y^n(i, j + 1/2, k), E_z^n(i, j + 1, k + 1/2)$ and $E_z^n(i, j, k + 1/2)$, along with its own value at $t = n - 1/2$. The new value of the field component at any lattice point can be determined independently at a given time instant. This allows the computational procedure to be fully vectorizable and is well suited for parallel processing.

During the simulation, the propagator is applied to the total field and therefore reflections that are generated by the discontinuities in the geometry at a given time step will become an integral part of the simulation at a later step. The ability to analyze reflection is a very powerful feature of the FDTD method. Unlike other simulation methods such as BPM which simulate wave propagation in the forward sense, the FDTD method preserves the complete information of the interaction between the wave and the geometry during its simulation.

3.3 Stability Criterion.

The *stability criterion*, the condition imposed on the ratio between the space and time increments, arises from the choice of the time-explicit differencing scheme. This condition is referred as the *Courant-Friedrichs-Lewy* (CFL) condition [20], which simply states that a differencing scheme cannot be convergent if the domain of dependence of a point in the finite differencing scheme does not include all points in the domain of dependence of the governing differential equation.

Consider the space-time diagram in Fig. 3, where each row of points on the diagram corresponds to the sampling points in space at a given instant of time. The shaded area contains the past history of the value at point $(k; n)$, such that it is determined in part by values at points $(k-1; n-1)$ to $(k+1; n-1)$. If this domain is a subset of the

differencing domain of dependency enclosed by the dashed lines, then the scheme is stable; otherwise, it is unstable with divergent results.

The stability criterion can be derived from a number of methods [5], and its role in the error analysis of the scheme will be further studied in the next section. In a sourceless and homogeneous medium, the stability criteria for multidimensional problems are [5]:

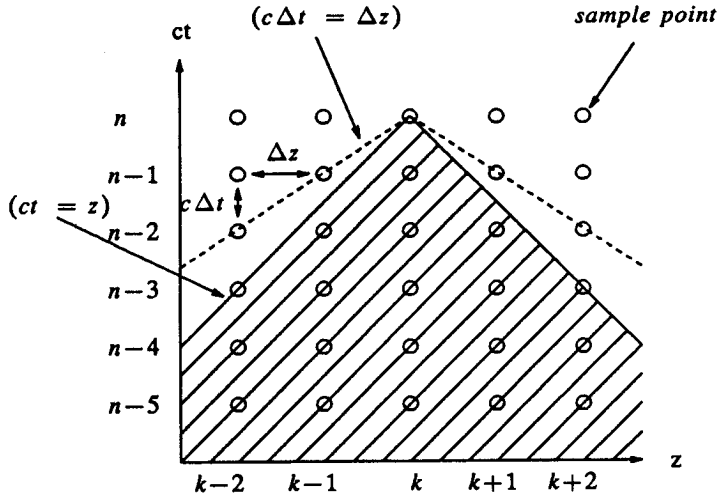

Figure 3. CFL condition for stability in one dimension.

$$1-D: \qquad v\Delta t \leq \Delta z \tag{25}$$

$$2-D: \qquad v\Delta t \leq \left[\frac{1}{\Delta x^2}+\frac{1}{\Delta z^2}\right]^{-1/2} \tag{26}$$

$$3-D: \qquad v\Delta t \leq \left[\frac{1}{\Delta x^2}+\frac{1}{\Delta y^2}+\frac{1}{\Delta z^2}\right]^{-1/2} \tag{27}$$

where v is the velocity of light in the medium. In the FDTD simulations, the value of v is chosen to be the maximum wave phase velocity expected within the model.

3.4 Numerical Error Analysis.

In addition to the roundoff errors associated with the finite representation of numbers in the computer, there is an additional source of error associated with the method. When simulating wave propagation on a discretized domain, a complex multiplicative factor γ is superposed onto the numerical solution. The induced error arises from the fact that a discretized domain is a dispersive propagating medium which is characterized by a frequency dependent phase velocity. Since the errors are propagating errors that increase with the number of time steps, these amplitude and phase distortions will play a important role in determining the accuracy of the solution.

The error associated with the numerically discretized simulation of wave propagation can be determined from the *von Neumann stability analysis* [19,21], or by a *Fourier analysis* [22]. A comprehensive discussion on the subject of numerical dispersion in the various differencing schemes is given in [23]. Here we will perform the von Neumann analysis to determine the γ of a one dimensional FDTD scheme. The procedure considers the simulation of propagation of a single frequency wave using the differencing scheme. It determines the complex amplitude γ imposed on the original waveform by the scheme. The analysis can only be applied on an nondissipative medium in which the amplitude of the solution remains constant. In one dimension, the FDTD differencing scheme with $\epsilon_{zz} = 1, \mu_{zz} = 1$ and $\sigma_{zz} = 0$ is:

$$\frac{\partial}{\partial \tau}\begin{bmatrix} H_y{}^n(k) \\ E_x{}^n(k) \end{bmatrix} = -\frac{\partial}{\partial z}\begin{bmatrix} 0 & 1 \\ 1 & 0 \end{bmatrix}\begin{bmatrix} H_y{}^n(k) \\ E_x{}^n(k) \end{bmatrix} \tag{28}$$

Assume that the solution to the above differencing scheme is

$$\begin{bmatrix} H_y{}^n(k) \\ E_x{}^n(k) \end{bmatrix} = \gamma^n e^{j\beta k \Delta z}\begin{bmatrix} H_y{}^0(0) \\ E_x{}^0(0) \end{bmatrix} \tag{29}$$

where the vector on the right-hand side is the exact initial condition, γ is a complex number, and β is the propagation constant in the medium. Substituting (29) into (28) yields the following system of equations:

$$\begin{bmatrix} 0 \\ 0 \end{bmatrix} = \begin{bmatrix} \gamma^{1/2} - \gamma^{-1/2} & -jR\sin(\theta) \\ -jR\sin(\theta) & \gamma^{1/2} - \gamma^{-1/2} \end{bmatrix} \cdot \begin{bmatrix} H_y{}^0(0) \\ E_x{}^0(0) \end{bmatrix} \tag{30}$$

where $\theta = \beta\Delta z/2$ and $R = c\Delta t/\Delta z$. The values of γ for the non-trivial solution in (30) are given by

$$\gamma = \exp\ j\left\{\tan^{-1} \pm \left[\frac{4R^2\sin^2(\theta) - 4R^4\sin^4(\theta)}{1 - 4R^2\sin^2(\theta) + 4R^4\sin^4(\theta)}\right]\right\} \tag{31}$$

provided R satisfies the CFL condition.

The error caused by the discretization can be determined from the magnitude and phase of γ. The magnitude of γ determines the spurious increase or decrease of the original wave amplitude. For this reason, it is called the *amplitude factor*. In the case of spurious increase when the factor is larger than unity, the system is unstable and the stability criterion will not be met. For the spurious decrease case, the high frequency components of the waveform will dissipate very quickly and the system fails to model these components.

The phase of γ will introduce a *phase factor* on the solution. This is the origin of the numerical dispersion in the differencing scheme. The amount of dispersion is determined by θ, which is a measure of the number of sample points in a wavelength. Generally, the ratio between the number of sample points and waveguide wavelength is $\gamma_g \geq 12\Delta z$, in order to ensure accuracy of the simulation.

Although γ in the FDTD scheme is complex and carries a phase factor, its magnitude is unity (see [5,21] for the proof of $|\gamma| = 1$ in three dimensions) and is independent of the ratio R provided it satisfies the CFL condition. The fact that there is no amplitude change is one of the advantages of the FDTD method.

3.5 Absorbing Boundary Conditions.

As mentioned in 3.2, the field component in the propagator is a function of its adjacent values. However, the computation region is finite and field values that are outside of the computation region will be needed if the propagator of (18)–(23) is used to calculate the nodes at the boundary. One can derive modified propagators for the boundary nodes that are functions of the nodes within the computation region only. The modified propagators are formulated from the various absorbing boundary conditions. These conditions assume wave that arrives at

the boundary is outgoing, so that the behavior of the wave is governed by the one-way equations [24–26]. The propagator for the boundary can be derived by expressing the one-way equation into its finite- difference form. However, the propagation constant of the outgoing wave in the one-way equation is not known. One has to approximate the value of the propagation constant. The order of the approximation corresponds to the order of the modified propagator, boundary condition. Some of the boundary condition used in the FDTD analysis are [5,11,27–32]. In general, to perfectly absorb an outgoing multifrequency wave at an arbitrary angle is difficult. The absorbing boundary conditions are usually not perfect and it will generate small spurious reflections at the boundary.

In the example presented in this chapter, the absorbing boundary condition proposed by [30] is found to be the most efficient. A brief derivation of this absorbing boundary condition will be presented in order to gain an understanding of the various approximations behind this and other boundary conditions.

Consider a truncation plane or boundary located at $x = 0$, with the computation region at $x \geq 0$. The absorbing boundary condition is needed to absorb the outgoing wave propagating in the $-x$ direction. The outgoing wave is assumed to be the plane wave solution to the scalar wave equation and can be expressed as:

$$\phi = \phi_0 \exp\left\{ j\left[\omega t + \beta_x x + \beta_y y + \beta_z z\right] \right\} \tag{32}$$

where β_x, β_y and β_z are the propagation constants in the x, y and z directions. Furthermore, with $k_0 = \omega/c$,

$$k_0^2 - \beta_x^2 - \beta_y^2 - \beta_z^2 = 0$$

or

$$\beta_x = k_0 \left\{ 1 - \frac{\beta_y^2}{k_0^2} - \frac{\beta_z^2}{k_0^2} \right\}^{1/2} \tag{33}$$

The expression (32) is differentiated with respect to x to obtain

$$\left[\frac{\partial}{\partial x} - j\beta_x\right]\phi = 0 \tag{34}$$

which is the governing equation for the absorbing boundary condition. If β_x is known, (34) explicitly relates $\phi(x = 0)$ with $\phi(x = \Delta x)$, so that values at the boundary can be determined without information from outside the region. The problem is to find the appropriate value for β_x In the second order boundary condition Mur [30] approximates (33) by

$$\beta_x \approx k_0\left[1 - \frac{1}{2k_0^2}({\beta_y}^2 + {\beta_z}^2)\right] \tag{35}$$

with error of the order $O\left[({\beta_y}^2 + {\beta_z}^2)^2\right]$

Let us pause now to analyze the sources of error in this and other absorbing boundary conditions. In order to explicitly express the values at the truncation boundary by the values within the computation region, one has to estimate the propagation velocity normal to the truncation plane. In this case, the value of β_x is determined from β_y and β_z. The error in the expression for β_x is related to the magnitude of β_y and β_z, with the accuracy of the expression inversely proportional to some order of β_y and β_z. This indicates that the boundary condition successfully absorbs paraxial waves traveling normal to the truncation boundary. As the wave direction starts to deviate from the axis and arrives at the boundary at a glancing angle, the spurious reflection from the boundary increases accordingly.

The approximate expression of β_x is substituted into (34), with jk_0 is replaced by the operator $\partial/\partial\tau$, to obtain:

$$\left\{\frac{\partial^2}{\partial\tau\partial x} - \frac{\partial^2}{\partial\tau^2} + \frac{1}{2}\left[\frac{\partial^2}{\partial y^2}\frac{\partial^2}{\partial z^2}\right]\right\}\phi = 0 \tag{36}$$

The difference expression for (36) evaluated at $x = 1/2$, $t = n$ is

$$\begin{aligned}\phi^{n+1}(0,j,k) = &-\phi^{n-1}(1,j,k) \\ &+ \frac{(c\Delta t - \Delta x)}{(c\Delta t + \Delta x)}\left[\phi^{n+1}(1,j,k) + \phi^{n-1}(0,j,k)\right] \\ &+ \frac{2\Delta x}{c\Delta t + \Delta x}\left[\phi^{n}(1,j,k) + \phi^{n}(0,j,k)\right] + \frac{(c\Delta t)^2 \Delta x}{2(c\Delta t + \Delta x)} \\ &\cdot \left\{\frac{1}{\Delta y^2}\left[\phi^{n}(1,j+1,k) + \phi^{n}(0,j+1,k) - 2(\phi^{n}(1,j,k)\right.\right. \\ &\left. + \phi^{n}(0,j,k)) + \phi^{n}(1,j-1,k) + \phi^{n}(0,j-1,k)\right] \\ &+ \frac{1}{\Delta z}^2\left[\phi^{n}(1,j,k+1) + \phi^{n}(0,j,k+1) - 2(\phi^{n}(1,j,k)\right. \\ &\left.\left. + \phi^{n}(0,j,k)) + \phi^{n}(1,j,k-1) + \phi^{n}(o,j,k-1)\right]\right\}\end{aligned} \tag{37}$$

Typically, the reflection from the truncation boundary using the second order boundary condition amounts to about 3% for normal incident, where the waveguide is perpendicular to the truncation plane. The total amount of reflection increases when the waveguide axis is no longer normal to the truncation plane. However, the propagation direction of the reflected signal now differs from the axial direction of the waveguide, thus the coupling of the reflection to the waveguide is small. The absorbing boundary condition is only required for the field components parallel to the truncation plane. The perpendicular components can be evaluated from these parallel components. A similar expression for the boundary condition for the edges and corners can be derived by assuming the directions for the wave.

The treatment of outgoing waves at the truncation boundary is critical in the analysis of structures in an open region. Improper boundary conditions will introduce spurious reflections that distort the proper solution. Readers should consult with references [24–26,30,31] for a better understanding of the operation and formulations of the different absorbing boundary conditions.

3.6 Source Excitation, Total Field, and Reflected Field Regions.

In this subsection we will present the methodology in defining a $+z$ propagating incident waveform. We will separate the computation region into two subregions, the *total field region* and the *reflected field region.* The plane separating these regions is called the incident plane. In the total field region, structures of interest such as a junction or more complicated structures are defined. The interaction between the incident wave and the waveguide geometry will take place in this region so that its field quantities must retain the information of both the incident and scattered waves. In the reflected field region, there are no junctions or discontinuities and the field quantities in this region are the reflections from the total field region. Since there are no discontinuities in this region, these signal will not be reflected back into the total field region.

The excitation scheme of a $+z$ propagating incident waveform consists of a total field region and a reflected field region that are located at $z \geq 0$ and $z \leq 0$, respectively. One can consider that the incident field is being generated by a flashlight located on the incident plane facing the $+z$ direction. The flashlight is turned off for $t \leq 0$ and the field values in the whole computation region are equal to zero. At $t = 0$ the flashlight is turned on and illuminates only the total field region. If the excitation scheme is perfect, there should not be any light detected by an observer located in the reflected region, unless there are some obstacles such as discontinuities in the total field region which would generate the reflection.

The incident wave can be generated by specifying the exact field distribution on the incident plane at each time interval. However, along with the required incident waveform, this method also generates the z propagating *parasitic waves.* The characteristics of these undesired waves are investigated using a Fourier analysis in [33], where it is shown that these are the backward solutions to the discretized wave equations and that their wavelengths, λp, are in the interval $2\Delta z > \lambda p > 4\Delta z$. These parasitic waves can reflect off the end boundary and propagate into the total field region. This can affect the accuracy of the solution.

In order to reduce the number of parasitic waves, the source is being excited into the waveguide geometry using the following procedure. Consider the two-dimensional transverse electric (TE) computation mesh in Fig. 4, where the total field region is located at $z \geq k$ and the reflected field region is located at $z < k$. The incident

plane is denoted by the dashed line. The evaluation of $E_y{}^n(i,k)$ and $H_x{}^{n+1/2}(i,k1/2)$, using the FDTD propagator, requires knowledge of the preceding half time step values of the field components across the incident plane. In order to ensure consistency during the computational procedure, the incident field $H_{x,inc}^{n-1/2}$ is added to $H_x{}^{n-1/2}(i,k-1/2)$ in the difference equation for $E_y{}^n(i,k)$ When calculating the value for $H_x{}^{n+1/2}(i,k-1/2))$, which is in the reflected field region, the incident field $E_{y,inc}^n$ is subtracted from $E_y{}^n(i,k)$ in the difference equation for $H_x{}^{n+1/2}(i,k-1/2)$. The subtraction of the incident field at the incident plane is necessary to reduce the amount of parasitic waves and enhance the dynamic range of the FDTD scheme.

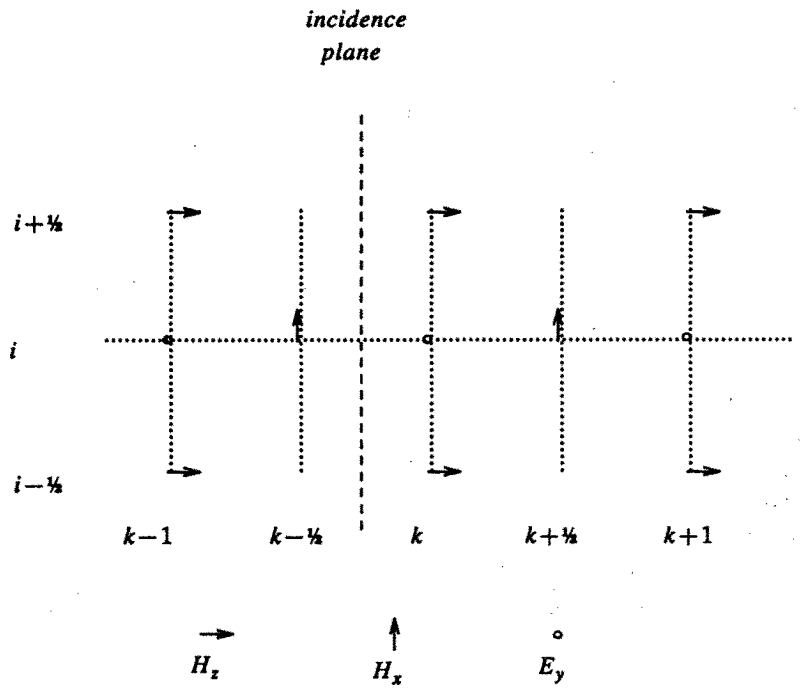

Figure 4. Source excitation condition in a 2- D TE mesh.

The source excitation scheme is not limited to generating only the $+z$ propagating incident wave. In continuous wave (CW) excitation, the time dependence of the incident field is a single-frequency sinusoidal function, so that:

$$\phi_{inc}(i, k_{inc}; t) = \phi_{inc}(i, k_{inc}) \sin(nk_0 c\Delta t + \theta_i) \tag{38}$$

where $k_0 = 2\pi/\lambda_0$ and where λ_0 is the wavelength of the optical signal. The initial phase offset θ_i is the phase difference between points in the incident plane. This offset can be adjusted to define the direction of the incident field. Eq. (38) is often multiplied by a taper function:

$$s(t) = 1 - \exp\{-t/\tau\} \qquad t > 0 \tag{39}$$

where τ is a time constant to reduce the transient effect. In pulse excitation, expression (38) is modulated by a slowly varying envelope function. For the Gaussian pulse, the envelope function is:

$$G(t) = \exp\left\{-\left[\frac{(nc\Delta t - T_0}{w}\right]^2\right\} \tag{40}$$

where T_0 is the time offset and w is the pulse width parameter.

3.7 Data Interpretation.

The result obtained from the FDTD simulation procedure described in the preceding section is the set of field values on the discretized region at the sampled time intervals. However, one would like to express the form of solution in the optical waveguide analysis in term of the power distributions or modal expressions. Using the simple example of wave propagation in a slab waveguide, the conversion from the large amount of raw data to the desired modal parameters of interest will be discussed in this section.

3.7.1 Propagation in a dielectric slab.

The dielectric slab considered in this example is shown in Fig. 5, and has the following waveguide parameters: $d = 0.3\,\mu m, n_0 = 1$ and $n_1 = 1.5$. The guided modes supported by the geometry are the TE_0, TE_1, TM_0 and TM_1 modes. Since the solution to the step-index

waveguide can be determined analytically, the exact field distribution of the slab waveguide is used as the incident wave. For arbitrary graded index or three-dimensional structures where the exact field distributions of the guided modes are difficult to obtain, the propagation characteristic of the structures must be predetermined by approaches such as the WKB [34] or finite-element method [35–37]. For convenience, we consider only the CW simulation of the TE mode propagation, where E_y, H_x, and H_z are the nonzero field components. The computation region in this example consists of 80×100 cells, with the mesh defined in $1 < i < 80$; $1 < k < 100$. The incident plane is located at $k = 40$. The increments used are $\Delta x = \Delta z = 2c\Delta t = 0.5\,\mu m$. As a first example, the $+z$ propagating TE_0 mode at $\lambda_0 = 1\mu m$ is launched from the incident plane at $t = 0$, that is at $n = 0$. The power carried by the incident field is normalized to one unit, so that $P_0 = |A_0|^2 = 1$ where A_0 is the normalized TE_0 modal amplitude. The E_y distributions along the z-axis ($i = 40$) at time steps $n = 40$, 120 and 400 are shown in Fig. 6. The response to the excitation of the geometry is characterized by the transient at the leading edge of the waveforms at $n = 40$ and 120. In order to obtain steady-state values at a given location it is necessary to wait until this transient has passed. The waveform at $k < 40$ is the parasitic wave generated by the excitation condition described in the previous section.

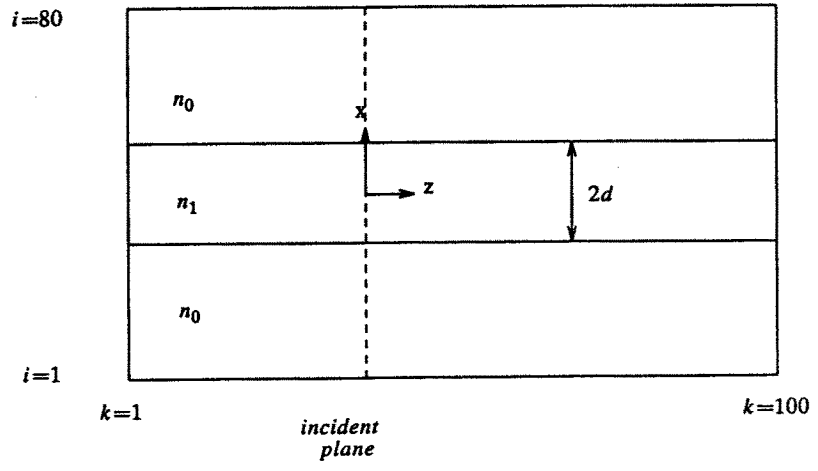

Figure 5. The dielectric slab waveguide.

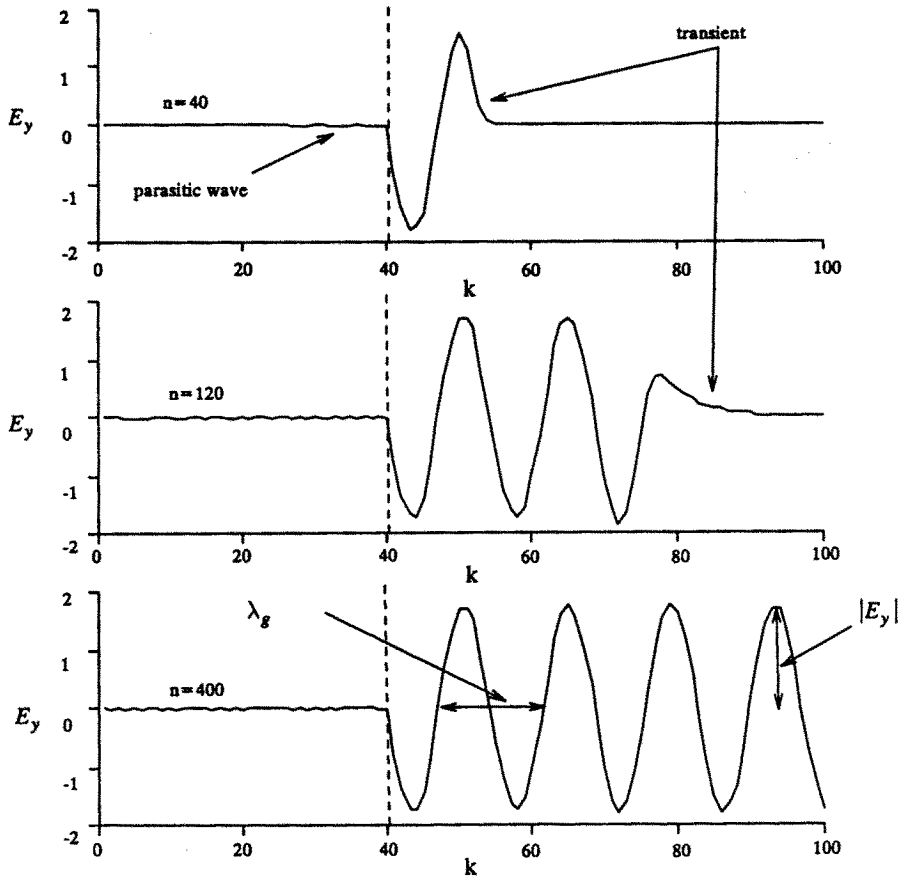

Figure 6. Plot of E_y vs z at various time steps.

There are a number of ways to determine the steady-state amplitude $|E_y|$ of the field component at a given location. The most direct way is to monitor the field values at the location and record the maximum and minimum values at each time step. The peak-to-peak amplitude can be evaluated from the difference between the extremum values. When using this approach, the recording should start after the transient has passed; therefore, it is necessary to calculate the peak-to-peak value for each time cycle until the value becomes constant. Another approach is to assume that the simulation has reached the steady-state and there is only a phase difference of $k_0 c\Delta t$ between the field values obtained form two consecutive time steps. Here, the unknowns are the magnitude and phase of the complex amplitude of the field component. With the two field values it is possible to determine these unknowns.

The advantages of this method are that it requires only two consecutive values to provide both the phase and magnitude of the field component. The calculation can be performed at the very last time step so that it requires much less computation time and it is not necessary to assign additional memory for recording the previous values. Due to its simplicity, this will be the approach used in all of the analyses for determining the steady-state results. However, when applying this method, one must note that if the amplitudes are calculated before the steady-state has been reached, the values from two consecutive time steps no longer differ by a phase constant. The resulting amplitude will be influenced by the improperly defined phase difference. This method is also very sensitive to numerical noise. In situations where there are noise problems, such as near the truncation boundaries, more sampling points would be needed to obtain a stable field amplitude.

3.7.2 Power distribution.

To show the power distribution in the slab at a given time instant, the instantaneous Poynting vectors $\vec{S}(\vec{r};t)$ at n = 400 are plotted for each cell,for $21 < i < 59$, $47 < k < 61$, and are shown in Fig. 7, where:

$$\vec{S}(\vec{r};t) \times \vec{H}(\vec{r};t) \tag{41}$$

The length of the vector is scaled linearly according to its magnitude. The z-dimension of Fig. 7 spans approximately one waveguide wavelength. Notice that these vectors are not all pointing in the z direction;

instead, they show the direction of the instantaneous power flow at each lattice point. The pattern is time dependent and moves to the right as a function of time. The energy is confined by the slab within the envelope of Poynting vectors and propagates along the axial direction.

Using the method described in the previous section, the time-averaged Poynting vectors $\vec{S}_{ave}(\vec{r})$ can be determined by first calculating the steady-state amplitudes for all the field components. Then $\vec{S}(\vec{r})$ is evaluated by:

$$\vec{S}_{ave}(\vec{r}) = \frac{1}{2} Re\left\{ \vec{E}(\vec{r};t) \times \vec{H}^{*}(\vec{r};t) \right\} \tag{42}$$

The time-averaged Poynting vector distribution over the same region as in Fig. 7 is shown in Fig. 8. In this case all the Poynting vectors point in the z-direction, showing the guiding characteristic of the TE_0 mode. Furthermore, the magnitude of the power consists of only one peak along the transverse x direction, indicating that it is the fundamental TE_0 mode. The amount of power carried by the TE_0 mode in the slab can be calculated by taking the surface integral of $\vec{S}_{ave}$ over a given transverse plane.

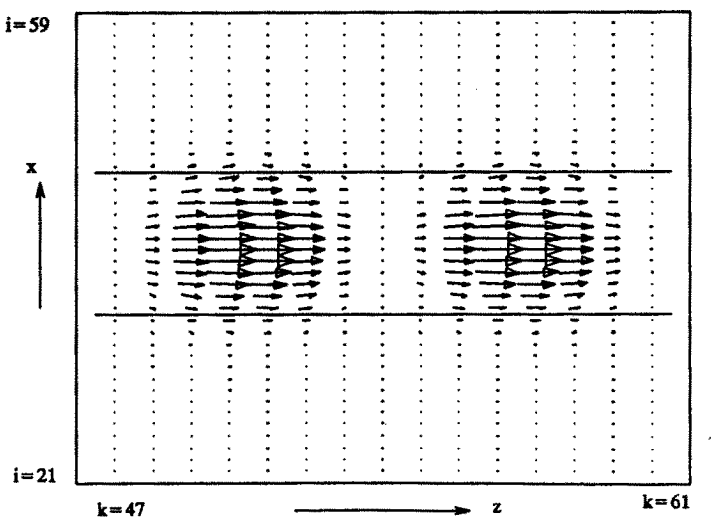

Figure 7. $\vec{S}(t)$ **distribution in the slab, with** TE_0 **incident.**

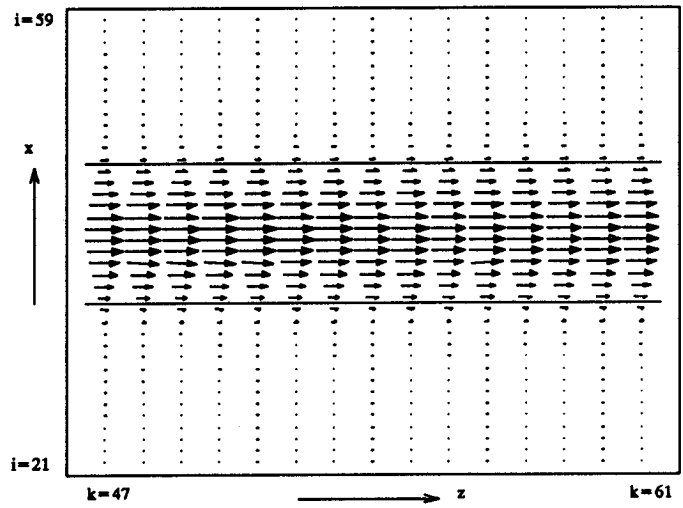

Figure 8. $\vec{S}(t)$ **distribution in the slab, with** TE_0 **incident.**

3.7.3 Modal Extraction.

If the power in the slab is carried by only one guided mode then the surface integral of $\vec{S}_{ave}$ over the transverse plane is the power in that mode. The situation becomes more complex if it is necessary to determine the power carried by the guided mode which is combined with the radiation modes and other guided modes.

Consider the multimode propagation in the slab where the incident waveform is the superposition of the te_0 mode with $A_0 = 1$, the TE_1 mode with $A_1 = 1/\sqrt{2}$, and also consider that these modes are in phase at the incident plane. The incident waveform is shown in the Fig. 9a and the time-averaged power distribution is shown in Fig. 9b. The power distribution shows the beat pattern between the two modes. At a given transverse plane, the power distribution is a combination of the modes with a certain phase difference. As a result, the distribution repeats itself after a distance L, where:

$$\frac{2\pi}{L} = \beta_0 - \beta_1 \tag{43}$$

and where β_0 and β_1 are the propagation constants of the TE_0 and TE_1 modes, respectively.

3.7.4 Least Squares Approach.

In order to determine A_0 and A_1 from the power distribution, it is necessary to calculate the overlap integral between the waveform distribution and the field distribution of the desired guided mode.

The process of separating the modal components in a waveform is performed numerically using the least squares approach [38]. Consider the steady-state solution in an optical waveguide analysis. In the least squares approach, the field distribution at a given point (i,k) in the computation region is considered to be the combination of the finite number of guided modes and a continuous spectrum of radiation modes. The field distribution is expressed as:

$$E^T(x_i, z_k; t) = \mathrm{Re}\left\{\sum_{l=1}^{N} A_l(z_k;t)E_l^g(x_i) + \int_0^\infty Q(\kappa_s)E^r(x_i)d\kappa_s\right\} \quad (44)$$

where

$$A_l(z_k;t) = A_l \exp\left\{j\left[\omega t - \beta_l z_k + \theta_l\right]\right\} \quad (45)$$

and where E^T, E^g and E^r are the total, guided and radiation field distributions, respectively, A and Q are the complex amplitudes of the guided and radiation modes, β_l is the propagation constant of the l^{th} guided mode and N is the number of guided modes in the waveguide. The solution of the FDTD simulation is in the form of the total field distribution, E^T. The problem is to determine A from E^T.

Here, we seek the least squares solution to Eq. (44), that is; the minimization of

$$|R|^2 = \sum_{l=0}^{M} |E^T(x_i) - \sum_{l=1}^{N} A_l E_l^g(x_i)|^2 \quad (46)$$

where M is the number of sampling points in the x direction. At a given instant $t = t_0$ and at plane $z = z_0$, the discretized form of (44) can be written as:

$$T = [G]b + R \quad (47)$$

where

$$T_i = E^T(x_i), G_{i,l} = E_l^g(x_i), b_l = \mathrm{Re}A_l \quad (48)$$

and R is the radiation field distribution. The minimization of (46) becomes:

The solution of (49) in the least squares sense is the estimated amplitude distribution. Equation (49) can be solved by a number of methods, such as by the singular-value decomposition approach [39]. Since the normal modes of the waveguide, including the integral of the continuous spectrum, are orthogonality to each other, the system is very stable. Notice that the resulting R is orthogonal to the vectors in [G], which corresponds to the orthogonal condition between the integral of the continuous radiation spectrum and each of the guided modes.

As described earlier, in order to determine the magnitude and phase of A_l, one needs to evaluate b_l at $t = t_0$ and $t_0 + \Delta t$. The magnitude A_l and phase $\omega t_0 - \beta_l z_0 + \theta_l$ can be obtained from (45). Once the complex amplitudes of the guided modes are determined, the radiation field distribution R can be determined directly from Eq. (46).

For structures with canonical waveguide cross-sections as input and output, where the guided mode distributions are well defined, the above technique can be applied to determine the energy distribution in the guided modes and in the radiation modes. However, even if the geometry of the input and output are arbitrarily shaped, such as in tapered waveguides, this technique can still be used to determine the power distributions of the local normal modes at a given transverse plane.

Using the above technique, the modal amplitudes A_0 and A_1 for the simulation in Fig. 9 are extracted and their magnitudes and phases are shown in Fig. 10a and 10b, respectively. The ripples on the curves in Fig. 10a correspond to the noise in the system from the sources described in the previous sections. The ripples are filtered out by fitting a straight line (shown as the dashed lines) through the data points. The extracted magnitudes $|A_0|$ and $|A_1|$ are 1.00 and 0.707, respectively. Since the uniform waveguide contains no axial discontinuity, the magnitudes of the modes are the same as the values excited at the input plane. The accuracy of the method can be estimated from the plot of modal phase versus axial distance, where the slopes of the lines correspond to the propagation constants β_0 and β_1. In this case, the percentage error for the extracted β_0 and β_1 are 0.81% and 0.77%, respectively.

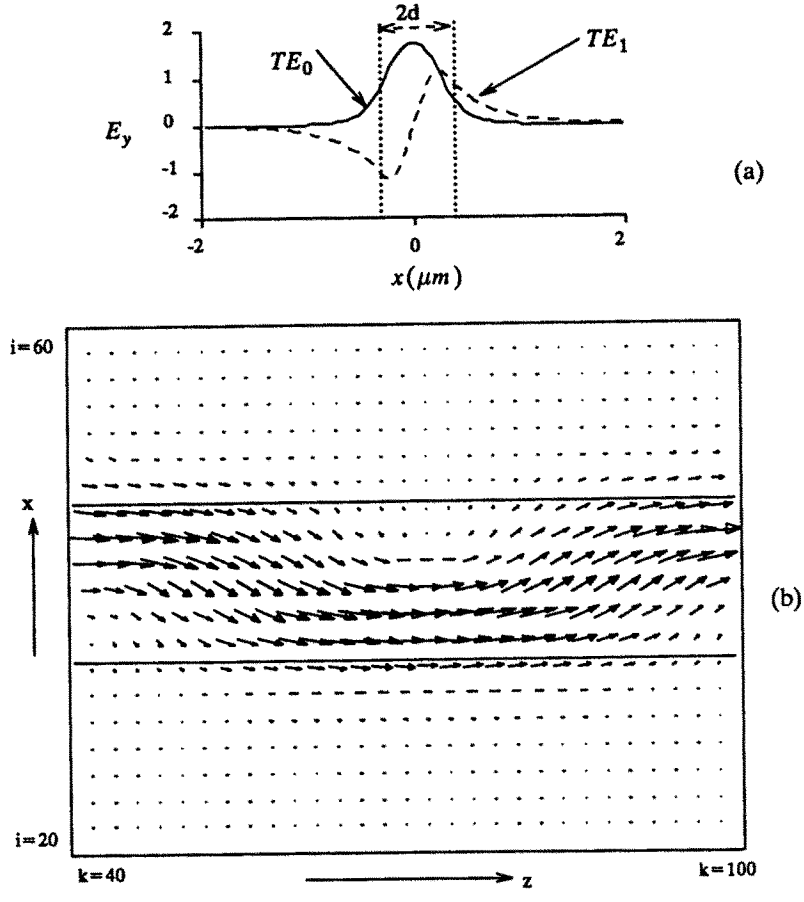

Figure 9. $|\overrightarrow{S}_{ave}|$ **distribution in the slab, with** TE_0 **and** TE_1 **incident.**

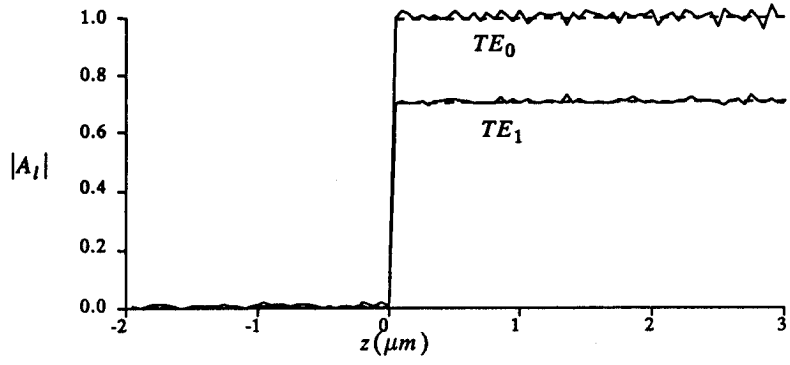

(a)

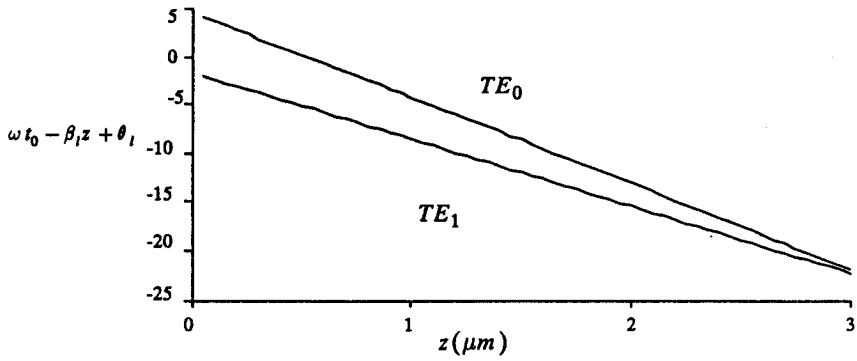

(b)

Figure 10. Extracted modal amplitudes from Figure 9 vs. axial distance.

4. The Scalar and Semi-Vectorial FDTD Algorithms

The method of extracting the modal amplitudes from the total fields compresses the vast amount of information generated by the FDTD algorithm into simple expressions that can be interpreted directly in the more interesting form of power distributions. It is interesting to see that although the algorithm calculates all the field component values, only the distribution of one field component is needed to determine the modal amplitude. In principle, one can solve a particular waveguide problem by determining only the distribution of the dominant field component. This is especially true in the case of optical guided-wave problems where the field intensity, $|\overrightarrow{E}|^2$, is proportional to the power distribution.

Due to the extensive computational requirement of the basic FDTD algorithm, the scalar and semi-vectorial FDTD algorithms have been developed to reduce the computational cost by analyzing only the propagation of the dominant field component. In the linear and inhomogeneous medium, the coupled Maxwell's curl equations are combined to form the vector wave equations:

$$\mu\epsilon\frac{\partial^2\overrightarrow{E}}{\partial t^2} = \nabla^2\overrightarrow{E} - \nabla^2\left[\nabla\frac{1}{\epsilon}\cdot\epsilon\overrightarrow{E}\right] \tag{50}$$

$$\mu\epsilon\frac{\partial^2\overrightarrow{H}}{\partial t^2} = \nabla^2\overrightarrow{H} + \nabla\epsilon\times\left[\frac{1}{\epsilon}\nabla\times\overrightarrow{H}\right] \tag{51}$$

If the electric field is linearly polarized in the x direction, where the dominant field components are E_x and H_y then both the x component of Eq. (50),

$$\begin{aligned}\mu\epsilon\frac{\partial^2 E_x}{\partial t^2} = {} & \frac{\partial^2 E_x}{\partial y^2} + \frac{\partial^2 E_x}{\partial z^2} + \frac{\partial}{\partial x}\left[\frac{1}{\epsilon}\frac{\partial}{\partial x}\epsilon E_x\right] \\ & + \frac{\partial}{\partial x}\left[\frac{1}{\epsilon}\frac{\partial\epsilon}{\partial y}E_y\right] + \frac{\partial}{\partial x}\left[\frac{1}{\epsilon}\frac{\partial\epsilon}{\partial z}E_z\right]\end{aligned} \tag{52}$$

and the y component of Eq. (51),

$$\mu\epsilon\frac{\partial^2 H_y}{\partial t^2} = \frac{\partial^2 H_y}{\partial y^2} + \epsilon\frac{\partial}{\partial x}\left[\frac{1}{\epsilon}\frac{\partial H_y}{\partial x}\right] + \epsilon\frac{\partial}{\partial y}\left[\frac{1}{\epsilon}\frac{\partial H_y}{\partial z}\right]$$

$$+\frac{\partial \epsilon}{\partial x}\frac{1}{\epsilon}\frac{\partial H_x}{\partial y}+\frac{\partial \epsilon}{\partial z}\frac{1}{\epsilon}\frac{\partial H_z}{\partial y} \tag{53}$$

can be used to describe the propagation of the field exactly. The terms involving the minor components $\frac{\partial}{\partial x}\left[\frac{1}{\epsilon}\frac{\partial \epsilon}{\partial y}E_y\right]$, $\frac{\partial}{\partial x}\left[\frac{1}{\epsilon}\frac{\partial \epsilon}{\partial z}E_z\right]$, $\frac{\partial \epsilon}{\partial x}\frac{1}{\epsilon}\frac{\partial H_x}{\partial y}$ and $\frac{\partial \epsilon}{\partial z}\frac{1}{\epsilon}\frac{\partial H_x}{\partial y}$ are the polarization coupling terms between the dominant and the minor components. In order to account for polarization effects, equations for the minor components similar to (52) and (53) are needed to form two sets of three second order differential equations. One can solve either one of these sets of simultaneous equations to determine the full vector behavior.

In the semi-vectorial approximation, the optical signal is assumed to be linearly polarized, and the polarization couplings are neglected. Furthermore, the interfaces between the difference indices are assumed to be parallel to the x and y directions. After eliminating the polarization coupling terms, the resulting equations are the semi-vectorial wave equations (SVWEs):

$$\mu\epsilon\frac{\partial^2 E_x}{\partial t^2}=\frac{\partial^2 E_x}{\partial y^2}+\frac{\partial^2 E_x}{\partial x^2}+\frac{\partial}{\partial x}\left[\frac{1}{\epsilon}\frac{\partial}{\partial x}\epsilon E_x\right] \tag{54}$$

$$\mu\epsilon\frac{\partial^2 H_y}{\partial t^2}=\frac{\partial^2 H_y}{\partial y^2}+\epsilon\frac{\partial}{\partial x}\left[\frac{1}{\epsilon}\frac{\partial H_y}{\partial x}\right]+\epsilon\frac{\partial}{\partial z}\left[\frac{1}{\epsilon}\frac{\partial H_y}{\partial z}\right] \tag{55}$$

The discontinuities of the normal $\vec{E}$ field and the tangential $\vec{H}$ field at the dielectric interfaces are considered by these equations. This allows the SVWEs to predict the propagation characteristics of the vector wave.

For two-dimensional problems where $\frac{\partial}{\partial y}$, Eqs. (54) and (55) reduce to the following propagating equations in the TM case:

$$\mu\epsilon\frac{\partial^2 E_x}{\partial t^2}=\frac{\partial^2 E_x}{\partial z^2}+\frac{\partial}{\partial x}\left[\frac{1}{\epsilon}\frac{\partial}{\partial x}\epsilon E_x\right] \tag{56}$$

$$\mu\epsilon\frac{\partial H_y}{\partial t^2}=\epsilon\frac{\partial}{\partial x}\left[\frac{1}{\epsilon}\frac{\partial H_y}{\partial x}\right]+\epsilon\frac{\partial}{\partial z}\left[\frac{1}{\epsilon}\frac{\partial H_y}{\partial z}\right] \tag{57}$$

Notice that (57) is exact for linear, nondispersive and isotropic medium. However, (56) neglects the couplings between the E_x and E_z components so that it is valid only for uniform structures in the z direction.

The TE SVWEs with the E_y and H_x components can be derived in the similar way. Notice that the SVWEs with E_y and H_x components describe the exact behavior of the TE and TM propagation of the optical signal In an isotropic region.

When the refractive index changes are small, $\nabla\epsilon \approx 0$, the scalar approximation [40] can be applied, then the SVWEs reduce to the scalar wave equation (SWE):

$$\nabla^2\psi - \frac{n^2}{c^2}\frac{\partial^2}{\partial t^2}\psi = 0 \tag{58}$$

where ψ represents the dominant field component. For the x polarized wave in this example, ψ can either be E_x or H_y.

In the semi-vectorial (SV) and scalar (S) FDTD algorithms [41,42], the SVWEs and the SWE are solved numerically using the finite-difference approach. An explicit time-domain approach similar to the basic FDTD algorithm is used to solve the reduced wave equations. In this way, the majority of the advantages of FDTD analysis are maintained.

The reduced wave equations are second order equations with respect to time. In the modified algorithms, the field values at the two previous time steps, $t = n-1$ and $t = n$, must be known in order to calculate the field value at $t = n+1$. Therefore, it is necessary to allocate computer memory to store the field values at $t = n$ and $t = n-1$. However, with only one unknown field component, the total required storage in the modified algorithms is smaller than in the basic FDTD algorithm. Using the same procedure as [19], it can be shown that the stability criterion for the S-FDTD algorithm is the same as (27). For the SV-FDTD algorithm to be stable the time increment must satisfy:

$$v\Delta t \leq \left[\frac{T_i}{\Delta x^2} + \frac{T_j}{\Delta y^2} + \frac{T_k}{\Delta z^2}\right]^{-1/2} \tag{59}$$

where (59) , $T_{i,j,k}$ are the maximum of the harmonic means of the refractive indices at the interfaces. The indices i, j and k correspond to the interface is parallel to the x, y and z direction, respectively. Here, $T = 1$ when the electric field is tangential to or the magnetic field is normal to the interface, otherwise,

$$T_{l\pm1} = \frac{2\epsilon(l \pm 1)}{\epsilon(l) + \epsilon(l \pm 1)}, \qquad l = i, j, k \tag{60}$$

For optical guided-wave problems in two dimensions, there is only one dominant field component and no polarization couplings; these modified algorithms are sufficient to describe the propagation behavior of the optical signal. In terms of computational costs, these algorithms require approximately 30% less memory and 50% less computational time then the basic algorithms for the two dimensional problems.

5. Extended FDTD Algorithms

In a medium where the constituent law relating E and D is more complex, it is necessary to use the more general expression of Maxwell's equations:

$$\nabla \times \vec{\varepsilon} = -\overleftrightarrow{\mu} \frac{\partial \vec{\mathcal{H}}}{\partial t} \tag{61}$$

$$\nabla \times \vec{\mathcal{H}} = \frac{\partial \vec{\mathcal{D}}}{\partial t} + \overleftrightarrow{\sigma}\, \vec{\varepsilon} \tag{62}$$

assuming $\vec{\mathcal{B}} = \mu_o \vec{\mathcal{H}}$. The extension to the FDTD algorithms must now establish the constituent relationship between $\vec{D}$ and $\vec{E}$ in the time domain so that it can be incorporated into the formulation. In the following sections, the extended FDTD algorithms in a time-varying and dispersive medium will be presented.

5.1 FDTD in a Time Varying Medium.

In the FDTD algorithm for media with extrinsically induced time varying refractive indices, such as by electro-optical and acousto-optical effects. The Maxwell's equations that are used in the basic FDTD algorithm are modified by incorporating the instantaneous relationship between the electric flux density and the electric field

$$\vec{\mathcal{D}}\,(t) = \overleftrightarrow{\epsilon}(t)\ \vec{\varepsilon}\,(t) \tag{63}$$

into Eq. (62) so that

$$\vec{\nabla} \times \vec{\mathcal{H}} = \overleftrightarrow{\epsilon}(t) \frac{\partial \vec{\varepsilon}}{\partial t} + \vec{\sigma}'\,(t)\ \vec{\varepsilon} \tag{64}$$

where

$$\overleftrightarrow{\sigma}'(t) = \frac{d\overleftrightarrow{\epsilon}(t)}{dt} + \overleftrightarrow{\sigma}(t) \tag{65}$$

The modified equation is then discretized in the usual way to yield the propagator. Note that when calculating the field components using the modified propagator, the values of ϵ and $\frac{d\epsilon}{dt}$ at each time step are required.

We will use the time varying FDTD algorithm to demonstrate the band limitation of a traveling wave Mach-Zehnder modulator. The limitation is due to the velocity mismatch between the optical and the rf signals. The schematic of a scaled down modulator is shown in Fig. 11, where β_m, ω_m are the rf wave propagation constant and frequency, respectively, and β_0 and ω_0) , are the optical wave propagation constant and frequency, respectively. The waveguide parameters are: $n_1 = 1.6, n_0 = 1.5, \Delta n = 0.02, L = 19\,\mu m$, $\theta = 2.86°$, and $d = 1\,\mu m$. The simulations were performed in two dimensions; for the TE case, at $\lambda = 1.3\,\mu m$ and $\omega_0 = 28\,\omega_m$. The computational mesh consists of 3000 by 200 grid points, with increments $\Delta x = \Delta z = 0.05\,\mu m$ and $c\Delta t = 0.025\,\mu m$. The intensity distributions of the modulator after 10000 time steps are shown in Fig. 12 for $\beta_0/\beta_m = 1$, 2/3, and 1/2. In Figure 12a, the optical signal travels at the same speed as the rf signal. The optical signals see the same index distribution along the parallel section of the modulator and there are no frequency limits on the modulation. As a result, sharp and distinct pulses are formed at the output of the modulator. As the degree of mismatch increases, as shown in Fig. 12b and 12c, the pulses begin to smear into each other and so the modulation is reduced. In order to measure the modulation for the various mismatches, the power distributions along the output branch of the modulator are shown in Fig. 13. These curves are obtained using the modal extraction techniques as described in the last section. The modulation depths calculated from the simulation results for $\beta_0/\beta_m = 1$, 1/2, and 1/3 are at 100%, 80.4%, and 7.8%, respectively. Note that the maximum power of the pulses are below one unit; the loss is due to the radiation and reflection at the waveguide transitions.

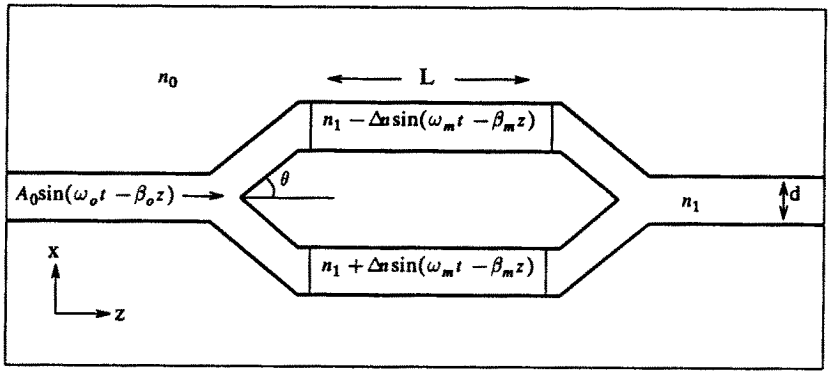

Figure 11. Schematic of the traveling wave Mach-Zehnder modulator.

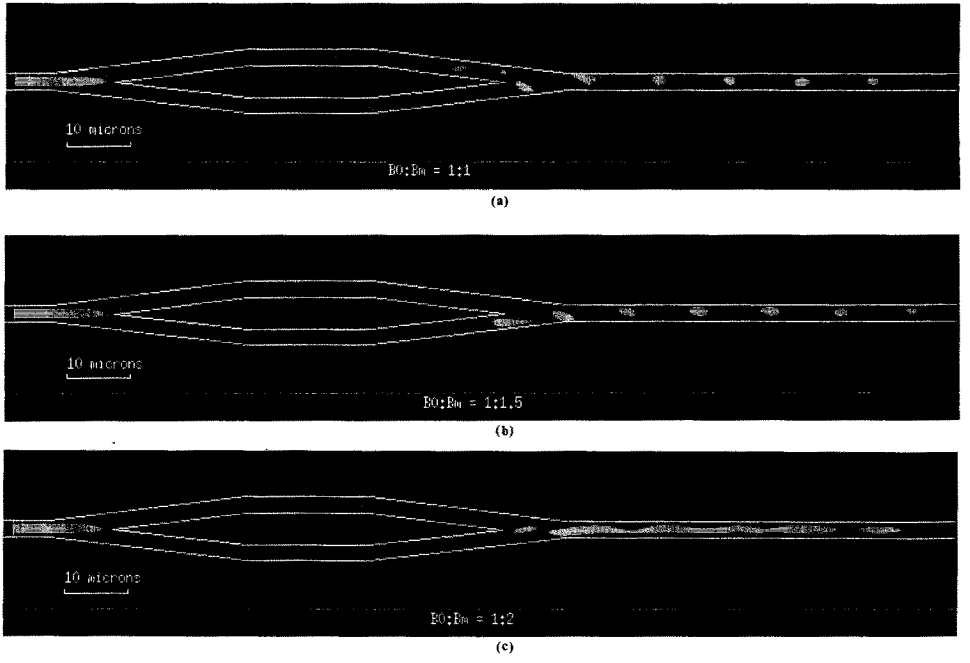

Figure 12. Intensity distributions of the modulator after 10000 time steps.

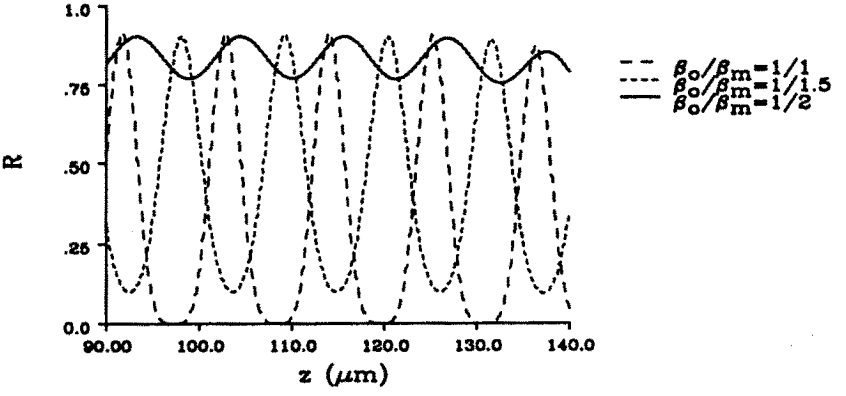

Figure 13. Spatial distributions of pulses at the output of the modulator.

5.2 FDTD in a Dispersive Medium.

In a linear dispersive medium the dielectric constant becomes a function of frequency. The electric flux density $\overrightarrow{D}$ is related to the electric field $\overrightarrow{E}$ by a linear integrodifferential equation:

$$D(t) = \epsilon_\infty \epsilon_0 E(t) + \epsilon_0 \int_0^t E(t-\tau)\chi(\tau)d\tau \tag{66}$$

Lubbers et al. [43] discretized the Debye dispersion relationship directly and incorporated it into the FDTD formulation. The discrete convolution method was later extended to media with multiple second-order Lorentz poles describing the complex permittivity [44].

Joseph et al. [45] proposed an alternative approach, the differential approach, to extend the FDTD method into a linear dispersive medium. The dispersion relationship $\epsilon(\omega) = \frac{D(\omega)}{E(\omega)}$ is converted into a differential equation by taking the inverse Fourier transform on both sides. The resulting differential equation is expressed as its difference form and added into the FDTD formulation that relates $\overrightarrow{D}$ and $\overrightarrow{E}$. The differential approach is more intuitive but may require more computer storage [44].

For most optical materials, the dispersion curve is expressed by the Sellmeier equation:

$$\epsilon(\omega) = \epsilon_\infty + \sum_{i=1}^{N} \frac{\epsilon_{s,i}}{\omega^2 - \omega_i^2} \tag{67}$$

In the wavelength range of interest, the dispersion curve can be fitted to the a Sellmeier equation with $N = 1$:

$$\epsilon(\omega) = \epsilon_\infty + \frac{\epsilon_{s,1}}{\omega^2 - \omega_1^2} \tag{68}$$

Following the approach used in [45], a differential equation is obtained by taking the inverse Fourier transform of the dispersion relationship:

$$\left[\frac{d^2}{\partial t^2} + \omega_1^2\right] D(t) = \left[\epsilon_\infty \frac{d^2}{dt^2} + (\epsilon_\infty \omega_1^2 - \epsilon_{s,1}\right] E(t) \tag{69}$$

In the extended FDTD algorithm, the differential equation is expressed in the difference form:

$$E^{n+1} = \left[2 + \frac{\Delta t^2}{\epsilon_\infty}(\epsilon_{s,1} - \epsilon_\infty \omega_1^2)\right] E^n - E^{n-1} \tag{70}$$

$$+\frac{1}{\epsilon_\infty}\left[D_{n+1} + D^{n-1} + (\Delta t^2 \omega_1^2 - 2) D^n\right] \tag{71}$$

and used to evaluate the value of E^{n+1}. The value of D^{n+1} is calculated by using either the curl equation of(62), or the general form of the semi-vectorial equation:

$$\mu \frac{\partial^2 \overrightarrow{D}}{\partial t^2} = \nabla^2 \overrightarrow{E} - \nabla\left[\nabla \frac{1}{\epsilon} \cdot \epsilon \overrightarrow{E}\right] \tag{72}$$

We will use the FDTD algorithm for a dispersive medium to evaluate the reflective spectra of a grating structure. This example will also demonstrate the use of pulse excitations in the FDTD analysis. Fig. 14 shows the volume grating to be analyzed. The gratings are assumed to be made of pure silica having the dispersion relationship near $\lambda = 1.3\,\mu m$:

$$n^2(\lambda) = A + \frac{B\lambda^2}{\lambda^2 - C^2} \tag{73}$$

where $B = 0.89748$ and $C = 9.89616$ are constants for all the materials, and $A = 2.00000, 2.08010$, and 2.10933 for n_s, n_f, and n_+, respectively. The grating period A is equal to $0.4545\,\mu m$ which corresponds to the first order grating length at $\lambda = 1.3\,\mu m, \Lambda = \beta/\pi$. The thickness of the film d is at $2\,\mu m$, and there are 100 gratings. We will perform the simulation for both distributed feedback (DFB) and distributed Bragg resonator (DBR) filter structures. The DBR has a phase shift region of $\lambda/4$ at the middle of the structure.

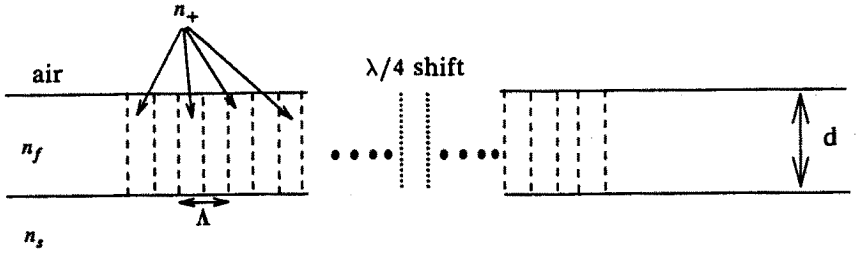

Figure 14. Schematic of the volume grating.

In the simulation, the input pulse is sent into the grating structure. The reflected pulse is then collected and analyzed to determine the characteristic of the filter. The temporal and axial distributions of the incident pulse are Guassian. The transverse distribution of the pulse has the form of a TE_0 mode profile. The central wavelength of the pulse λ_0 is at $1.3\ \mu m$ and the pulse width is at $12\lambda_0$. When choosing the pulse width, one must be aware of that the high frequency components of the pulse, which may violate the stability criterion. The effect of these distortion can produce noise that affects the spectrum of interest. In practice, pulse widths larger than $10\lambda_0$ should be used.

The temporal distribution of the input pulse is shown in Fig. 15. The reflection is monitored by performing the modal extraction of the TE_0 distribution on the instantaneous field values in the reflected region. A typical reflected signal is shown in Fig. 16. The reflection in this case is for a structure with only 20 gratings, and corresponds to the cumulative reflections from each of the gratings. For a structure with more grating periods, the reflected pulse train is correspondingly

longer. In principle, the reflected signal must be taken from $t = 0$ to $t = x$. However, the reflected signal after the third or fourth reflection is usually very weak and the data gathering can be terminated at that point. One should also subtract the backward propagating parasitic wave from the reflected signal. As mentioned earlier, the parasitic wave is generated by imperfect excitation conditions. Although the noise created by the wave may be small, it can reduce the dynamic range of this method. The noise can be determined by observing the reflections in the simulation of a uniform structure. Since the structure should not produce any reflections due to the geometry, the reflection it does generate is the numerical reflection caused by the source excitation. Finally, the reflected spectra for the grating structures are obtained by taking the transfer function between the Fourier transform of the reflected signal and the input signal. The reflected spectra for the DFB and DBR filters for the example here are shown in Fig. 17.

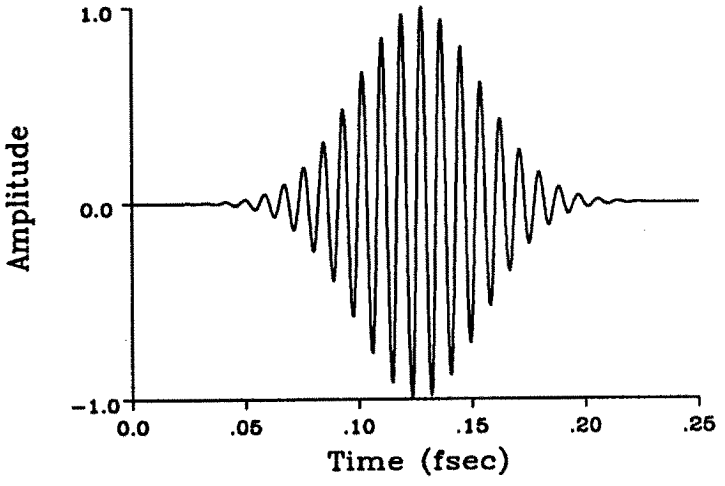

Figure 15. The input Gaussian pulse used in the analysis of grating structures.

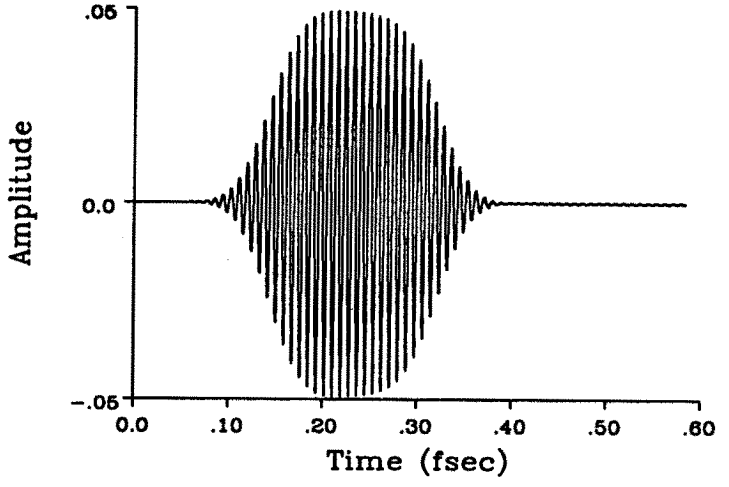

Figure 16. The reflected pulse train from the grating structure with 20 periods.

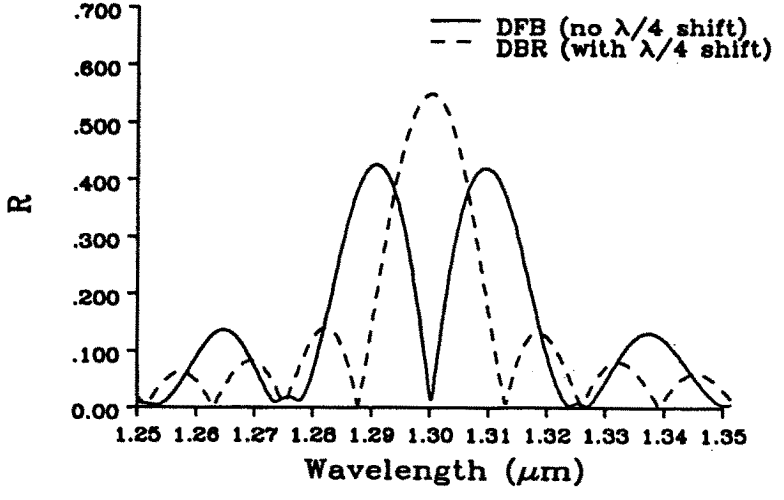

Figure 17. The reflected spectra of the DFB and DBR grating structures.

6. Conclusion

In summary, the FDTD method is a very versatile and powerful method for the analysis of electromagnetic wave interactions. It is well suited for the analysis of compact geometries having strong wave interactions or having weak but extended interactions that can add up coherently. Current researches are focussed on the improvement of the efficiency of the method, such as the S-FDTD and SV-FDTD, and to extend the FDTD algorithm to more complex media, such as dispersive and nonlinear media. The method has begun to gain popularity amongst the researchers in optical modeling and simulation. Recently, in the 1993 Integrated Photonics Research meeting at Palm Springs, California, a section was devoted for the development of the time domain method .

Acknowledgments

This work was supported in part by a grant from the Canadian Institute for Telecommunication Research under the NCE program of the Government of Canada and in part by the Information Technology Research Center, an Ontario Provincial Center of Excellence.

References

1. Yee, K. S., "Numerical solution of initial boundary value problems involving Maxwell's equations in isotropic media," *IEEE Trans. Antennas Propagat.*, Vol. AP-14, 302–307, 1966.
2. Goorjian, P. M., and A. Taflove, "Direct time integration of Maxwell's equations in nonlinear dispersive media for propagation of femtosecond electromagnetic solitons," *Opt. Lett.*, Vol. 17, 180–182, 1992.
3. Goorjian, P. M., A. Taflove, R. M. Joseph, and S. C. Hagness, "Computational modeling of femtosecond optical solitons from Maxwell's equations," *IEEE J. Quantum Electron*, Vol. QE-28, 2416–2422, 1992.
4. Ziolkowski, R. W., and J. B. Judkins, "Linear-Nonlinear interfaces: results from Full-Wave, vector Maxwell's equation NL-FDTD simulations," *1993 Integrated Photonics Research Technical Digest*, Vol. 10, 128–131, 1993.

5. Taflove, A., and M. E. Brodwin, "Numerical solution of steady-state electromagnetic scattering problems using the time-dependent Maxwell's equations," *IEEE Trans. Microwave Theory Tech.*, Vol. 23, 623–630, 1975.
6. Taflove, A., "Review of the formulation and applications of the finite-difference time-domain method for numerical modeling of electromagnetic wave interactions with arbitrary structures," *Wave Motion,* Vol. 10, 547–582, 1988.
7. Umashankar, K. R., and A. Taflove, "A novel method to analyze electromagnetic scattering of complex objects," *IEEE Trans. Electromagn. Compat.*, Vol. EMC-24, 397–405, 1982.
8. Taylor, C. D., D. H. Lam, and T. H. Shumpert, "Electromagnetic pulse scattering in time-varying inhomogeneous media," *IEEE Trans. Antenna Propagat.*, Vol. AP-17, 585–589, 1969.
9. Merewether, D. E., "Transient currents induced on a metallic body of revolution by an electromagnetic pulse," *IEEE Trans. Electromagn. Compat.*, Vol. EMC-13, 41–44, 1971.
10. Holland, R., L. Simpson, and K. S. Kunz, "Finite-difference analysis of EMP coupling to lossy dielectric structures," *IEEE Trans. Electromagn. Compat.*, Vol. EMC-22, 203–209, 1980.
11. Zhang, X., J. Fang, K. K. Mei, and Y. Liu, "Calculations of the dispersive characteristics of microstrips be the time-domain finite-difference method," *IEEE Trans. Microwave Theory Tech.*, Vol. MTT-36, 263–267, 1988.
12. Chu, S. T., and S. K. Chaudhuri, "A Finite-difference time-domain method for the design and analysis of guided-wave optical structures," *IEEE J. Lightwave Technol.*, Vol. LT-5, 2033–2038, 1989.
13. Chu, S. T. "Modeling of guided-wave optical structures by the finite-difference time-domain method," *Ph.D. Thesis*, Dept. Elect. Eng., University of Waterloo, 1990.
14. Chu, S. T. S. K. Chaudhuri, and W. P. Huang, "Simulation and analysis of waveguide based optical integrated circuits," *Computer Physics Communications*, Vol. 68, 451–484, 1991.
15. Lee, S. M., W. C. Chew, M. Moghaddam, M. A. Nasir, S. L. Chuang, R. W. Herrick, and C. L. Balestra, "Modeling of rough-surface effects in an optical turning mirror using the finite-difference time-domain method," *IEEE J. Lightwave Tech.,* Vol. LT-9, 1471–1480, 1991.

16. Kimmel, J. S., and D. A. Christensen, "Finite-difference time-domain modeling and experimental characterization of planar waveguide fluorescence sensors equation NL-FDTD simulations," *SPIE Chemical,* Biochemical, and Enviromental Fiber Sensors 111, 1587, 136–146, 1991.
17. Hawkins, R. J., N. K. Madsen, J. S. Kallman, M. D. Feit, C. C. Shang, B. W. Shore, and J. F. DeFord, "Full-wave simulations of the thumbtack laser," *l993 Integrated Photonics Research Technical Digest,* Vol. 10, 116–119, 1993.
18. Sano, E., and T. Shibata, "Fullwave analysis of picosecond photoconductive switches," *IEEE J. Quantun Electron.,* Vol. QE-26, 372–377, 1990.
19. Press, W. H., B. P. Flannery, S. A. Teukolsky, and W. T. Vetterling, *Numerical Recipes*, Cambridge University, Cambridge 1986.
20. Lakshmikantham, V., and D. Trigiante, *Theory of Difference Equations: Numerical Methods and Applications*, Academic Press, Boston, 1988.
21. Choi, D. K., "A Development of hybrid FD-TD/TLM method and its application to plannar millimeter wave waveguide structures," *Ph.D. Thesis*, Dept. Elect. Eng., University of Ottawa, 1986.
22. Vichnevetsky, R., *Wave Propagation Analysis of the Box and Other Implicit Approximations of Hyperbolic Equations*, Tech. Report Dept. Comp. Sci., Rutgers University, 1986.
23. Trefethrn, L. N., "Group velocity in finite difference schemes," *SIAM Review,* Vol. 24, 113–137, 1982.
24. Engquist, B., and A. Majda, "Absorbing boundary conditions for the numerical simulation of waves," *Math. Comp.,* Vol. 31, 629–651, 1977.
25. Trefethen, L. N., and L. Halpern, "Well-posedness of one-way equations and absorbing boundary conditions," *Math. Comp.,* Vol. 47, 421–435, 1986.
26. Higdon, R. L., "Absorbing boundary conditions for difference approximations to the multi-dimensional wave equation," *Math. Comp.,* Vol. 47, 437–459, 1986.
27. Holland, R., and L. Simpson, "Finite-difference analysis of EMP coupling to thin struts and wires," *IEEE Trans. Electromagn. Compat.,* Vol. EMC-23, 88–97, 1981.

28. Bayless, A., and E. Turkel, "Radiation boundary conditions for wave-like equations, *Commun. Pure Appl. Math.*, Vol. 33, 707–725, 1980.
29. Kriegsmann, G. A., A. Taflove, and K. R. Umashankar, "A New formulation of electromagnetic wave scattering using an on-surface radiation boundary condition approach," *IEEE Trans. Antennas Propag.*, Vol. AP-35, 153-160, 1987.
30. Mur, G., "Absorbing boundary conditions for the finite-difference approximation of the time-domain electromagnetic field equation," *IEEE Trans. Electromagn. Compat.*, Vol. EMC-23, 377–382, 1981.
31. Fang, J., and K. K. Mei, *A Super-absorbing boundary algorithm for solving electromagnetic problems by the time-domain finite-difference method, IEEE AP-S and URSI Symp.*, Syracuse, June 1988.
32. Liao, Z. P., H. L. Wong, B. Yang, and Y. Yuan, "A Transmitting boundary for transient wave analysis," *Scientia Sinica (Series A)*, Vol. 37, 1063–1076, 1984.
33. Vichnevetsky, R., "Energy and group velocity in semi discretizations of hyperbolic equations," *Math. Comput. Simulation*, Vol. 23, 333–343, 1981.
34. Okoshi, T., *Optical Fibers,* Academic Press, New York, 1982.
35. Davies, J. B., F. A. Fernandez, and G. Y. Philippou, "Finite element analysis of all modes in cavities with circular symmetry," *IEEE Trans. Microwave Theory Tech.*, Vol. MTT-30, 1975–1980, 1982.
36. Koshiba, M., H. Kazuya, and M. Suzuki, "Improved finite-element formulation in terms of the magnetic field vector for dielectric waveguides," *IEEE Trans. Microwave Theory Tech.*, Vol. MTT-33, 227–233, 1985.
37. Mabaya, N., P. E. Lagasse, and P. Vandenbulcke, "Finite element analysis of optical waveguides," *IEEE Trans. Microwave Theory Tech.*, Vol. MTT-29, 600–605, 1981.
38. Chu, S. T., and S. K. Chaudhuri, "Combining modal analysis and the FD-TD method in the study of dielectric waveguide problems," *IEEE Trans. Microwave Theory Tech.*, Nov. 1990.
39. Golub, G. H., and C. F. Van Loan, *Matrix Computation,* The Johns Hopkins University Press, Maryland, 1983.
40. Snyder, A. W., and J. D. Love, *Optical Waveguide Theory,* Chapman and Hall, London, 1983.

41. Huang, W. P., S. T. Chu, A. Goss, and S. K. Chaudhuri, "A Scalar finite-difference time-domain approach for guided-wave optics," *IEEE Photon. Technol. Lett.*, Vol. 3, 524–526, 1991.
42. Huang, W. P., S. T. Chu, and S. K. Chaudhuri, "A Semivectorial finite-difference time-domain approach for guided-wave optics, *IEEE Photon. Technol. Lett.*, Vol. 3, 803–806, 1991.
43. Lubbers, R., F. Hunsberger, and K. Kunz, "A Frequency-dependent time domain formulation for transient propagation in plasma," *IEEE Trans. Antennas Propag.*, Vol. AP-39, 29–34, 1991.
44. Lubbers, R., and F. Hunsberger, "FDTD for Nth-order dispersive media," *IEEE Trans. Antennas Propag.*, Vol. AP-40, 1297–1301, 1992.
45. Joseph, R., S. Hagness, and A. Taflove, "Direct time integration of Maxwell's equations in linear dispersive media with absorption for scattering and propagation of femtosecond electromagnetic pules," *Opt. Lett.*, Vol. 16, 1412–1414, 1991.